Elucidating the degradation mechanism of the cathode catalyst of PEFCs by a combination of electrochemical methods and X-ray fluorescence spectroscopy

Monzo Gimenez, Francisco Javier; van der Vliet, Dennis; Yanson, Alex; Rodriguez, Paramaconi

DOI:
10.1039/C6CP03795J

Elucidating the degradation mechanism of the cathode catalyst of PEFC by a combination of electrochemical methods and X-ray fluorescence spectroscopy

J. Monzó[1], D.F. van der Vliet[1], A. Yanson[2] and P. Rodriguez[1*]

[1] University of Birmingham. School of Chemistry, Birmingham. B15 2TT, UK.

[2] Cosine Measurement Systems, Oosteinde 36, 2361 HE Leiden. The Netherlands

Corresponding author: p.b.rodriguez@bham.ac.uk

Keywords: degradation mechanism, oxygen reduction reaction, platinum nanoparticles, X-ray fluorescence.

TOC

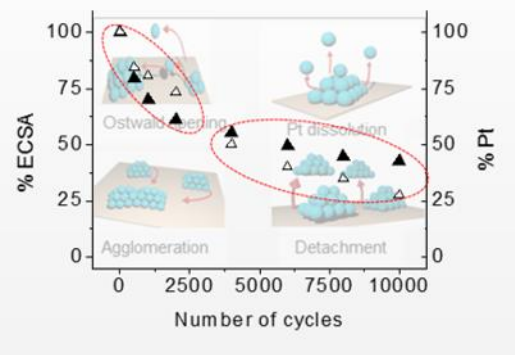

Abstract

In this study, we report a methodology which enables the determination of the degradation mechanisms responsible for catalyst deterioration under different accelerated stress protocols (ASPs) by combining measurements of the electrochemical surface area (ECSA) and Pt content (by X-ray fluorescence). The validation of this method was assessed on high surface area unsupported Pt nanoparticles (Pt-Nps), Pt nanoparticles supported on TaC (Pt/TaC) and Pt nanoparticles supported on Vulcan carbon (Pt/Vulcan). In the load cycle protocol, the degradation of Pt-Nps and Pt/ Vulcan follows associative processes (*e.g.*

agglomeration) in the first 2000 cycles, however, in successive cycles the degradation goes through dissociative processes such as Pt dissolution, as is evident by the similar decay of ECSA and Pt content. In contrast, the degradation mechanism for Pt nanoparticles dispersed on TaC occurs continuously through the dissociative processes (*e.g.* Pt dissolution or particle detachment), with similar decay rates of both Pt content and ECSA. In the start-up/shut-down protocol, high surface area Pt-Nps follow associative processes (*e.g.* Ostwald ripening) in the first 4000 cycles, after which the degradation continues through dissociative processes. On the other hand, dissociative mechanisms always govern the degradation of Pt/TaC under start-up/shut-down protocol conditions.

Finally, we report that Pt nanoparticles supported on TaC exhibit the highest catalytic activity and long term durability of the three nanoparticle systems tested. This makes Pt/TaC a potentially valuable catalyst system for the application in polymer electrolyte fuel cell cathodes.

Introduction

Polymer Electrolyte Fuel Cells (PEFCs) are proposed as a promising energy conversion technology for automotive applications due to their high theoretical energy efficiency, high power density, low working temperature, and low/zero emissions[1]. However, the durability of PEFCs is one of the main barriers for their commercialization[2–4]. As a consequence of the operating conditions, the cathode catalyst layer (*i.e.* Pt/Carbon) suffers harsh deterioration by means of both metal-catalyst (Pt or Pt-alloys) degradation[5] and carbon support oxidation[6]. This deterioration results in a loss of Electrochemical Surface Area (ECSA), and consecutively a rapid failure of the device[7].

In order to evaluate and to time-efficiently tackle the durability issues of the PEFCs, the Department of Energy (DOE) of the United States has designed accelerated stress protocols (ASPs)[8]. These degradation protocols have been designed to mimic the operating conditions during real-life application of a fuel cell. The two procedures in question are called the load cycle protocol (0.5 – 1.0 V *vs.* RHE), also called lifetime protocol[9], and the start-up/shut-down protocol, also called start/stop[10] (0.5 – 1.5 V *vs.* RHE). Even though these protocols help to assess the absolute durability of the catalyst over given time and conditions, they do not provide understanding of the complexity of the degradation process of the catalyst layer. In order to improve the durability of the PEFCs and design new catalysts, it is essential to understand the degradation mechanisms occurring at the cathode catalyst layer under operating conditions. The degradation processes of the metal-catalyst have been grouped in associative processes such as particle agglomeration[11] and Ostwald ripening[12]; or dissociative processes such as Pt dissolution[13] and particle detachment[14]. In addition to the metal-catalyst degradation, it is also known that the carbon support irreversibly oxidizes under certain conditions, resulting in isolation and detachment of the active metal nanoparticles[15,16].

One of the first attempts to elucidate the degradation mechanism of the cathode catalyst was reported by Mayrhofer *et al.*[14,17] The authors established a methodology which consists of monitoring the Pt/C catalysts by transmission electron microscopy (TEM) before (Beginning of Life, BOL) and after degradation protocols (End of Life, EOL). The authors simultaneously determine the ECSA and the nanoparticle size by TEM. In that study, the authors concluded that dissociative processes were the dominant degradation mechanisms of Pt/C, however, they were not able to conclusively establish whether the degradation was related to a detachment process,

or to the Pt dissolution process. By using identical location transmission electron microscopy (IL-TEM), Arán-Ais *et al.* have proposed that coalescence-agglomeration and migration processes are degradation mechanisms responsible for the Pt nanoparticles with deterioration under similar oxidative conditions[18]. In a relatively more complex system, Chen *et al.* used scanning transmission electron microscopy-X-ray energy dispersive spectroscopy (STEM EDS) to study the degradation of PtCo nanoparticles, however the authors were not able to distinguish between particle detachment or particle dissolution as sources of the catalyst degradation[19].

In a recent work, Sasaki *et al.* have attempted to determine the dissolution mechanism of Pt/C under oxidative conditions by using *in situ* electrochemical synchrotron-based X-ray absorption spectroscopy (XAS) and X-ray diffraction (XRD)[20]. The authors concluded that the dissolution of Pt occurs at potentials higher than 1.9 V *vs.* RHE, due to local high acidification caused by the oxygen evolution reaction and carbon corrosion. These results differ from those obtained by Mayrhofer *et al.*[21] who observed the Pt dissolution at potentials of around 1.15 V *vs.* RHE. These differences can be attributed to the different structure of both electrodes (*i.e.* supported nanoparticles in Sasaki *et al.* and extended Pt electrodes in Mayrhofer *et al.*). Finally, a comprehensive work of the degradation of Pt/C catalyst has been developed by Myer's group using SAXS[22,23]. In these works, the authors concluded that electrochemical cycling process results in significant particle growth and surface area loss. It is suggested that the decrease on the ECSA of the Pt catalyst is associated to the Pt dissolution or the detachment of the smallest particles, followed by re-deposition, thus resulting in particle growth. It is also suggested that beyond the critical size of approximately 3 nm Pt dissolution rates of the Pt slow considerably. It is important to note that these studies focus in different time scales

of the degradation process and neither of these studies include an exhaustive analysis of the degradation mechanism of the Pt nanoparticles and its correlation with catalytic activity towards the ORR as a function of time under ASPs in a complete time scale.

After reviewing these controversial results, the exact degradation mechanism as a function of time for the Pt-based catalysts remains unclear, as a consequence of the fact that the applied techniques are not able to distinguish between associative or dissociative processes taking place concurrently within the catalyst layer. In this work, we present a novel methodology which combines the measurement of the ECSA by electrochemical means, and the measurement of the Pt content in the catalyst layer using X-ray fluorescence (XRF). In contrast to the aforementioned results, the combination of both of these techniques allows discrimination between associative and dissociative degradation mechanisms of the Pt catalyst as a function of time.

This report presents the validation of the method for unsupported Pt nanoparticles, Pt nanoparticles supported on carbon and Pt nanoparticles supported on TaC. In addition, the effect of the catalyst degradation on the oxygen reduction reaction (ORR) activity has been assessed.

Pt nanoparticles supported on TaC were selected as a subject of study due to the reported chemical stability of the TaC and the predicted strong interaction between the Pt and the TaC [24]. Such a strong metal support interaction between the Pt and the TaC might favour the stability of the Pt nanocatalyst. On the other hand, unsupported catalysts such as Pt-alloy aerogels or metal thin films have shown improved durability towards electrochemical cycling [25–27] . The durability of this catalyst might be associated to the absence of support materials (the nanoparticles

avoid detachment upon cycling). However, the close interconnection between particles and the lack of dispersion might result in a fast Ostwald ripening or agglomeration. For a proper comparison, commercial and widely used Pt/Vulcan has been used as a standard.

1. Experimental section

1.1 Preparation of catalysts inks

Platinum nanoparticles were synthesized using the cathodic corrosion method in a 2-electrode configuration[28,29]. In brief, a well-known length of a Pt wire (Alfa Aesar 99.999%) was submerged in a solution of NaOH (1 M) and alternating cathodic potentials between -3 and 0 V were applied versus the Pt counter electrode, with a frequency of 100 Hz and a duty cycle of 50%, until all of the submerged wire was converted to black metal nanoparticles, dispersed in the solution. Afterwards, the solution was centrifuged at 3000 rpm for 20 minutes to precipitate the solids and remove the excess NaOH solution. Then, the Pt nanoparticles were redispersed in water (ElgaPureUltra 18.2 MΩ). This process was repeated 3 times until the pH was measured to be neutral. Because the synthesis does not utilize organic solvents or a capping agent, no further cleaning procedures are required[18,30,31,32].

A well-controlled amount of Pt nanoparticles were dispersed on TaC (Alpha Aesar) in order to obtain a catalyst with 20 wt.-% Pt with respect to the total mass of the catalyst. Briefly, an aqueous solution containing $(1.00 \pm 0.01) \times 10^{-2}$ M TaC was mixed with Pt nanoparticles and stirred for 24 hours. The resulting solution was centrifuged, the supernatant was discarded, and the solids dispersed in a given volume of ElgaPureUltra water in order to obtain a maximum concentration of 0.30 $g_{catalyst}$ /L.

As a reference catalyst, we have used Pt/Vulcan (20 wt.-% Pt) from ETEK. The BET surface area of the carbon Vulcan reported by the provider is 250 m^2/g. The catalyst ink was prepared by weighing out $(7.0 \pm 0.1) \times 10^{-3}$ $g_{catalyst}$ and dispersing it in 20 mL of ElgaPureUltra water, yielding a solution with a concentration of $(7.00 \pm 0.01) \times 10^{-2}$ g/L of Pt.

1.2 Physical characterization

The particle size distribution of Pt-Nps, TaC and Pt/Vulcan was determined by Transmission Electron Microscopy (TEM) using a JEOL JEM 1200 EX MKI instrument. The samples were prepared by drop-casting suspensions of each catalyst in isopropanol on carbon-coated copper grids and consecutively drying them in air.

The particle size and crystalline structure of the catalysts were obtained by X-ray diffraction (XRD). The XRD patterns were acquired using a Bruker AXS D2 PHASER diffractometer with Co-Kα (0.179 nm) radiation source. The samples were prepared by depositing a few drops (total volume 20 µL) of the catalyst on a zero background SiO holder (MTI), and drying the drops under Ar flow.

The compositional analysis of the catalyst`s layer was determined by XRF using a Bruker S8 Tiger 4kW spectrometer (see also supporting information, section 1).

The BET surface area of the TaC (1.34 m^2/g) was determined using a Quantachrome Quadrasorb equipment. Nitrogen sorption tests were measured at 77 K in N_2 atmosphere after degassing the samples at 120 °C under vacuum for 10 hours.

1.3 Sample preparation

In order to study the ECSA and the catalytic activity towards the ORR, the thin film method was employed in a rotating disk electrode (RDE) configuration [33,34,35]. The working electrode consisted of a disk of glassy carbon (diameter = 5 mm), on which a film of the catalyst was deposited to obtain a final loading of 30 $\mu g_{Pt}\,cm^{-2}$ [35]. It is crucial to obtain a homogeneous catalyst layer on the electrode, in order to have uniform O_2 diffusion, and accordingly an appropriate diffusion limited current, which is geometry dependent. Furthermore, a homogeneous catalyst layer is key to obtain accurate and reproducible results[36,37]. For this reason, the deposition of the catalysts on the carbon disk was performed by drop casting and drying several small aliquots of the catalyst suspensions, rather than a single large drop. The resulting homogeneous catalyst layer was confirmed microscopically (Figure SI1).

In this work, the catalyst layer has been prepared without Nafion to prevent oxygen transport resistance, electronic resistance and sulfonate adsorption. Kocha *et al.*[37] and Ohma *et al.* [38] reported the influence of Nafion on the electrocatalytic activity of Pt-based electrocatalysts, observing that the intrinsic activity of Nafion-cast catalysts is lower than the activity for Nafion-free catalysts due to the adsorption of the sulfonate anion from Nafion.

1.4 Electrochemical measurements

The electrochemical measurements were carried out in a two compartment electrochemical cell at room temperature with an Autolab PGSTAT12 potentiostat. A gold wire was used as counter electrode and a saturated calomel electrode (SCE) as reference electrode, although all the potentials are reported with respect to the reversible hydrogen electrode (RHE). The electrolyte solution was 0.1 M $HClO_4$ (Suprapure, Merck), prepared with ultra-pure water (ElgaPureUltra, 18.2 MΩ cm, 1 ppb total organic carbon).

1.5 Methodology for the evaluation of the catalyst degradation mechanisms under oxidative conditions

The durability of the catalysts was evaluated under two ASPs described by the DOE[39]: i) the load cycle protocol (cycling range between 0.5 to 1.0 V *vs.* RHE) for a total of 10000 cycles; and ii) the start-up/shut-down protocol (cycling range from 0.5 to 1.5 V *vs.* RHE during 5000 cycles). In both protocols, the catalyst was cycled in an air saturated solution 0.1 M $HClO_4$ at 50 mV/s. Initial studies performed in our laboratory showed that the formation/accumulation of bubbles under the RDE electrode (due to carbon oxidation to CO_2) might lead to inaccurate measurements of the ECSA and irreproducible results. Therefore, all the ASPs presented here were performed with 300 rpm rotation. After a defined number of degradation cycles, the ECSA and the ORR polarization curves were acquired in a fresh solution. In addition, the content of Pt and TaC left on the disk was determined by XRF. More details, as well as the calibration curves that establish the relationship between the net intensity signal and the mass of Pt or TaC, with its error propagation, are presented in the supporting information (Sections 3 and 4).

2. Results and discussion

2.1 Catalysts characterization

The Pt nanoparticles prepared by the cathodic corrosion were used in two separate ways: 1) as unsupported nanoparticles and 2) after being dispersed on TaC.

Figure 1A shows a TEM image of the Pt-Nps prepared by the cathodic corrosion method. The Pt nanoparticles present a particle size distribution of 5.2 ± 0.7 nm (Figure SI4). The XRD pattern at the 2Θ = 46.82º (111), 54.40º (200) and 80.79º (220) reflections confirms the presence of Pt nanoparticles (Figure 1C). Signals

associated to crystal structures of NaOH used during the synthesis were not detected, confirming the purity of the nanoparticles.

Figure 1B shows the TEM image of TaC crystals of about 300 nm, surrounded by clusters of ~5 nm Pt particles. It is important to notice that the dispersion of the Pt nanoparticles is limited by the low surface area of the TaC. The signals at 2Θ = 46.82º, 54.40º and 80.79º confirm the presence of Pt-Nps whilst the signals at 2Θ = 40.72º, 47.38º, 69.24º, 83.58º and 88.09º confirm the presence of TaC (Figure 1D). The composition of 19.6 % Pt and 80.4 % TaC was confirmed by XRF (Figure SI5).

The TEM images and the XRD pattern of the Pt/Vulcan are shown in Figure SI6. The TEM images confirm the presence of Pt nanoparticles with a particle size distribution of 4.8 ± 0.1 nm dispersed on porous carbon.

2.2 Determining the beginning of life conditions

Figure 2A shows the blank voltammetric profiles of Pt-Nps, Pt/TaC and Pt/Vulcan in 0.1 M $HClO_4$ solution. The unsupported Pt nanoparticles and the Pt nanoparticles supported on TaC present an almost identical voltammetric profile, which confirms that the Pt loading is the same in both cases. Furthermore, the figure corroborates the TEM images in showing that TaC has a relatively small surface area, as evident from the near-identical double layer region for these two catalyst systems. In contrast, the Pt/Vulcan exhibits a significantly larger double layer, due to the large surface area and porosity of the Vulcan carbon[40]. In all cases, the ECSA was determined by integrating the charge under the curve in the H_{upd} adsorption/desorption potential region (after double layer subtraction) and using the theoretical value of 210 μC cm_{Pt}^{-2} for the formation of a hydrogen monolayer[41]. The resulting values of the ECSA (Pt-Nps 53 ± 1 m_{Pt}^2 g^{-1}, Pt/Vulcan 57± 1 m_{Pt}^2 g^{-1} and

Pt/TaC 54 ± 1 $m_{Pt}^2\ g^{-1}$) are in agreement with the theoretical value obtained for spherical Pt nanoparticles with a particle size of 5 nm (55.85 $m_{Pt}^2\ g^{-1}$). This agreement conclusively shows that all the material on the disk is electrically connected and accessible to protons from the electrolyte.

Figure 2B shows the ORR polarization curves of the three catalysts in O_2-saturated 0.1 M $HClO_4$ solutions. The polarization curves of Figure 2B have been corrected by subtracting the background (capacitive and ionic adsorption processes present in the blank curves from Figure 2A), and have been Ohmic drop corrected[42]. Figure SI7 shows the Tafel plots for each catalyst. The intrinsic catalytic activity (j_k) of the catalysts at 0.9 V *vs.* RHE was calculated from the measured reduction current (j) and the diffusion current (j_d) according to the modified Koutecky - Levich equation (eq. 1)[43].

$$j_k = \frac{j_d \cdot j}{j_d - j} \qquad (1)$$

Table 1 summarizes the beginning of life (BOL) condition for each of the three samples. These results are in good agreement with previously reported ECSA and catalytic activity for Pt-based catalysts[44]. Pt/TaC shows a 1.3-fold improvement of specific activity and mass activity over Pt-Nps and Pt/Vulcan. The enhanced intrinsic activity of Pt nanoparticles supported on TaC could be associated with a Strong Metal Support Interaction (SMSI). The SMSI effect has been reported as being responsible for the enhancement of the activity of Pt nanoparticles, when supported on other transition metal carbides[45]. It is believed that by introducing early transition metal carbides as supports for Pt metals, there will be a slight increase in the 5d vacancy of Pt, resulting in a shift of the d band center of Pt, and therefore an increase the binding energy of O_2[24].

2.3 Degradation mechanisms of catalyst layer

Figure 3 shows the theoretical relationships between the ECSA and the Pt content during the Pt degradation. Figure 3A shows the first possible scenario in which the decay of the Pt content is larger than the decay of ECSA. This trend corresponds to a degradation process dominated by dissociative mechanisms such as Pt dissolution of particle detachment. The associative processes such agglomeration or Ostwald, is presented in Figure 3B where the decay of the ECSA is larger than the Pt content decay. A purely associative process would show loss of ECSA, while the Pt content would remain unchanged.

2.3.1 Load cycle protocol

Figure 4A-C compares the blank voltammetry of the three studied catalysts at BOL (t=0) and end of life (EOL, after 10000 cycles). The decrease of the H_{UPD} region and the platinum oxide region upon cycling is a clear indication of the degradation of the catalysts. Figure 4D summarizes the decay of the ECSA as a function of the number of cycles for the three catalysts. After 10000 cycles, the decrease of the surface area of the Pt-Nps (from 53 $m^2\ g^{-1}$ to 22 $m^2\ g^{-1}$) is comparable to the decrease of the surface area of Pt/Vulcan (from 57 $m^2\ g^{-1}$ to 25 $m^2\ g^{-1}$). On the other hand, the Pt nanoparticles supported on TaC clearly show a smaller decrease in ECSA (from 54 $m^2\ g^{-1}$ to 34 $m^2\ g^{-1}$). As was mentioned in the experimental section, the catalysts layers are prepared without ionomer. The effect of particle detachment, always a risk when no binder is used, has been studied by measuring the ECSA before and after a rotating stress protocol (300 rpm) at open circuit potential in 0.1 M $HClO_4$. The cyclic voltammetries of the catalysts before and after 5 hours under rotation (Figure SI8) show the stability of the catalyst without the Nafion film. Therefore, we conclude that losses of ECSA and Pt content are solely associated to electrochemical processes,

and that mechanical detachment of large clusters due to rotation of the electrode can be discarded.

It is interesting to note that the decrease of the surface area during the first 2000 cycles is much faster than the decrease in successive cycles. In order to investigate the causes for the decrease of the ECSA more in depth, we have determined the Pt content as a function of the number of cycles using XRF (Figure SI9).

ICP-MS measurements were performed on the solutions after each set of cycles using a (Agilent 7500ce instrument); however, the reported values presented large uncertainties. The uncertainty, although not confirmed, was likely mainly attributed to inhomogeneity of the sample. It is important to note that ICP-MS analysis provides information on the total platinum remaining in the solution, no matter the nature of the Pt (Pt ions and Pt nanoparticles). Even though the samples were placed in an ultrasonic bath for 5 minutes prior to the ICP–MS analysis, the precipitation of the nanoparticles in the sample vial and the retention on the Teflon tube and the Nebuliser nozzle could not be ruled out

Figure 5 compares the ECSA normalized by its initial value, and the similarly normalized Pt content for each catalyst as a function of cycle number. During the first 2000 cycles, the ECSA of the Pt-Nps decreases 40 % while the Pt content decreases 25 %. In keeping with the model (Figure 3), this trend is related to associative processes. In successive cycles, the decay of Pt content is larger than the decay of ECSA, which suggests that contrary to the first 2000 cycles, dissociative processes are now the dominant processes taking place. This behaviour of both ECSA and Pt decay fits perfectly with the theoretical model. Pt/Vulcan presents a similar trend: In the first 4000 cycles, the decrease in ECSA is 40 % and the decay of Pt is 30 %, meaning that associative processes are the predominant

mechanism for the Pt/Vulcan degradation. Carbon support oxidation has to be also considered in the degradation of Pt/Vulcan[15,46]. Similar decay for the ECSA and Pt content of Pt/Vulcan occurs in consecutive cycles, indicating behaviour related to dissociative processes. In contrast, to both Pt-Nps and Pt/Vulcan, Pt/TaC presents a proportional decrease of ECSA and Pt content in the first 4000 cycles, which suggests that dissociative processes such as Pt dissolution are at least equal to associative processes, if not prevalent. Furthermore, dissociative processes dominate the degradation of Pt/TaC catalyst after these 4000 cycles, as the decrease of the Pt content is larger than ECSA decay. This means that during the entire protocol, dissociative processes make up the bulk of the degradation mechanism. After completing the whole load cycle protocol, the ECSA of Pt/TaC remains 63 % of the initial value, in comparison with the 40% ECSA remaining on the Pt-Nps and the Pt/Vulcan. At the initial stages of the degradation process (between 0-2000 cycles), the Pt and Pt/Vulcan show an increase in the particle size which can be understood by an associative process (agglomeration/Ostwald ripening). This process was also observed by Gilbert et al. in a shorter time scale [23]. A more dramatic increase can be seen on the start-up/shut-down protocol. It can be seen that after an initial increase of the particle size, the average particle size decreases for both Pt and Pt/Vulcan. The change of the mechanism from associative to dissociative cannot be understood just from the point of view of the particle size but also from the point of view of other factors such as the dispersion of the nanoparticles. The surface density of the nanoparticles decreases as the particle size increases. The distance between the particles would results in a larger diffusion pathway of the Pt ions, resulting in a larger dilution of the Pt ions; thus, the growth mechanism and the Ostwald ripening is compromised while the dissolution

mechanism is favoured. This could be interpreted as a limited diffusion field of neighbouring nanoparticles. In addition, the presence of bigger/heavier nanoparticles in on the surface might also result in detachment. This mechanism would be consistent with a nucleation-aggregative growth-detachment type mechanism also observed in similar systems like nucleation and growth of Ag nanoparticles on HOPG[47].

Figure 6A-C shows the ORR polarization curves of the catalysts at different stages of the protocol. The onset of the reaction shifts to lower potentials as a consequence of the catalyst degradation. The effect of the degradation on the current density at 0.9 V *vs.* RHE is well defined on the Tafel plots (Figure SI11). Figure 6D shows the mass activity normalized by the mass activity at BOL as a function of the number of cycles. In the first 2000 cycles the mass activity of Pt-Nps decreases by 35 %, which is coherent with the observed decrease of ECSA, and attributed to associative degradation processes. In successive cycles, where the degradation was dominated by dissociative processes, the catalytic activity decreased by 32 %. Similar to the unsupported Pt-Nps, the Pt/Vulcan also exhibited a total loss of 70 %, with the Pt/TaC showing a slightly lower loss of its initial activity towards the ORR at 60 %. Perhaps the similar relative losses in mass activity indicate that the decay caused by the load cycle protocol results in a relatively stable state of the catalyst that is similar for all the catalyst systems tested. However, even though this relative decrease in activity with respect to the initial value is comparable, the Pt/TaC has a higher mass activity (0.142 A mg^{-1}) after 10000 cycles in comparison with the Pt-Nps (0.089 A mg^{-1}) and the Pt/Vulcan (0.079 A mg^{-1}).

2.3.2 Start-up/shut-down protocol

The blank voltammetry of the three catalysts at BOL and EOL for the start-up/shut-down protocol are shown in Figure 7A-C. As can be seen from Figure 7B, the signals associated to the H_{UPD} and PtO on the Pt/Vulcan completely disappeared after 2000 cycles. On the other hand, the unsupported Pt-Nps presented a better stability, as its initial ECSA only decreases from 53 m^2 g^{-1} to 17 m^2 g^{-1} after 2000 cycles, with complete degradation only after the entire protocol had run. Noteworthy, and in contrast with the other two catalyst, the voltammetric profile of the Pt/TaC still shows H_{UPD} and PtO signals after the 5000 start-up/shut-down cycles, with an ECSA of 21 m^2 g^{-1} at EOL. Figure 7D summarizes the change of the ECSA as a function of the number of cycles for the three catalysts, where the superior stability of the Pt/TaC catalyst is clearly on display.

Analogously to the load cycle protocol studies, the Pt content for each catalyst as a function of number of cycles was determined by XRF (Figure SI12), in order to determine the degradation mechanism of the catalyst. Figure 8 shows the normalized ECSA and Pt content (as in Figure 5) of the catalyst as a function of the number of cycles for each of the catalyst in this study. The degradation of the three catalysts is significantly higher than in the load cycle protocol. During the first 2000 cycles, the ECSA of the Pt-Nps, decreases 65 % and the Pt content decreases by 45 %, which confirms that the associative processes, such as Ostwald ripening, are responsible for Pt-Nps degradation. In successive cycles, the decay of ECSA and Pt content is proportional, suggesting that dissociative processes are the dominant degradation processes taking place.

The degradation mechanism of Pt/Vulcan is significantly different to the unsupported Pt-Nps, as in the first 1000 cycles the catalyst suffers a dramatic decrease of the ECSA of up to 75 % and the Pt content decreases by 48 %. The cause of this rapid

degradation could be directly explained by associative processes, if it was not for the fact that the process is more complex, since the carbon support corrosion also plays an important role[15,46]. In contrast, the degradation of Pt/TaC goes through dissociative processes, as evident by the 60 % decay of ECSA, and the 63 % drop in Pt content during the entire protocol. The decay rate of the Pt content is higher than during the load cycle protocol, owing to the faster dissolution of Pt as a consequence of the higher upper potential applied[20]. The average particle size was obtained for each cycle using the ECSA and the mass of platinum (Figure SI10). At the initial stages of the degradation process, between 0-1000cycles, the Pt and Pt/Vulcan shows a dramatic increase of the particle size which can be understood by an associative process (agglomeration/Oswald ripening). It can be seen, that after an initial increase of the particle size of the Pt-Nps decreases. As it was explained before, this change of the mechanism can be interpreted as a limited diffusion field of neighbouring nanoparticles. In addition, the presence of bigger/heavier nanoparticles in the surface might also result in detachment [47].

During the start-up/shut-down test, the TaC also suffers from degradation and the Ta content showed a decay of *ca.* 18 % (Figure SI13). This means that the degradation mechanism of Pt/TaC could be affected by the degradation of TaC. However, these results confirm that Pt/TaC catalyst presents substantially improved long term durability in comparison with the Pt-Nps and the Pt/Vulcan catalyst.

Figure 9A-C shows the ORR polarization curves of the catalysts through the start-up/shut-down protocol. The kinetic current of the Pt/Vulcan is the most affected, with a decrease of 61 % in the catalytic activity after only 1000 cycles (Figure 9D). Meanwhile, the onset of the ORR after 1000 cycles for the Pt-Nps and Pt/TaC shifts 12 mV and 6 mV (Figure SI14), respectively, resulting in decay of 37 % and 25 %

(Figure 9D). Figure 9D compares the normalized mass activity for each catalyst as a function of number of cycles. The mass activity of Pt-Nps drops rapidly by 77 % in the first 2000 cycles. This decrease is significantly higher than the 60 % decrease observed for the ECSA, highlighting the effect of the particle size change in the catalytic activity of Pt towards the ORR[48] .

The most severe decay in mass activity was observed on the Pt supported on Vulcan. As observed in Figure 7, the Pt/C Vulcan did not exhibit any H_{upd} after 2000 cycles, and therefore no catalytic activity was observed. Significant to mention is the stability of the mass activity of the Pt nanoparticles dispersed on TaC. The mass activity of Pt/TaC decreases by 47 % during the first 2000 cycles, but remains relatively stable during the next 3000 start-up/shut-down cycles. These results confirm that Pt nanoparticles supported on TaC are more stable and have better performance towards the ORR under severe oxidative conditions than Pt-Nps and Pt/Vulcan.

3. Conclusions

In this communication, we have reported a novel route to elucidate and distinguish between associative and dissociative degradation processes of metal catalysts under oxidative conditions. The deterioration of the catalysts exhibits an associated loss of ECSA and Pt content, the relative magnitude of which depends on the degradation mechanism. The reported methodology combines the measurement of ECSA by *in-situ* proton adsorption with *ex-situ* determination of the Pt content using in-depth X-ray fluorescence, allowing for the distinction between degradation mechanisms as a function of time during the entire degradation process.

Three different Pt-based catalysts have been prepared and characterised to validate the methodology. The stability and degradation of the catalysts have been studied carrying out two ASPs, with the catalysts presenting clearly different degradation mechanisms during the complementary protocols. Pt-Nps presented predominantly associative mechanisms such as particle agglomeration, as opposed to the dissociative processes such as Pt dissolution, which were the main degradation mechanisms for Pt/TaC.

This methodology is postulated as a powerful tool to assess the degradation mechanisms of the catalysts under oxidative conditions. In contrast with other methodologies, it not only allows us to determine the degradation mechanism, but also simultaneously links this to the decrease of the catalytic activity towards the ORR. The results obtained using this methodology are valuable as a standard procedure for the design of new cathode catalysts with improved long term durability for PEMFCs applications.

4. References

1 C. Song, *Catal. Today*, 2002, **77**, 17–49.

2 Y. Shao, G. Yin and Y. Gao, *J. Power Sources*, 2007, **171**, 558–566.

3 R. Borup, J. Meyers, B. Pivovar, Y. S. Kim, R. Mukundan, N. Garland, D. Myers, M. Wilson, F. Garzon, D. Wood, P. Zelenay, K. More, K. Stroh, T. Zawodzinski, J. Boncella, J. E. McGrath, M. Inaba, K. Miyatake, M. Hori, K. Ota, Z. Ogumi, S. Miyata, A. Nishikata, Z. Siroma, Y. Uchimoto, K. Yasuda, K.-I. Kimijima and N. Iwashita, *Chem. Rev.*, 2007, **107**, 3904–51.

4 F. Buchi, M. Inaba and T. J. Schmidt, *Polymer electrolyte fuel cell durability*, New York, Springer., 2009.

5 S. Zhang, X.-Z. Yuan, J. N. C. Hin, H. Wang, K. A. Friedrich and M. Schulze, *J. Power Sources*, 2009, **194**, 588–600.

6 L. M. Roen, C. H. Paik and T. D. Jarvi, *Electrochem. Solid-State Lett.*, 2004, **7**,

A19.

7 L. Carrette and K. A. Friedrich, *ChemPhysChem*, 2000, **1**, 162–193.

8 http://energy.gov /sites/prod/files/2015/08/f25/ fcto _dwg _usdrive_ fctt_ accelerated_stress_tests_jan2013.pdf, *U.S. DRIVE Fuel Cell Tech Team*, 2013.

9 X.-Z. Yuan, H. Li, S. Zhang, J. Martin and H. Wang, *J. Power Sources*, 2011, **196**, 9107–9116.

10 T. J. Schmidt and J. Baurmeister, *J. Power Sources*, 2008, **176**, 428–434.

11 Y. Shao-Horn, W. C. Sheng, S. Chen, P. J. Ferreira, E. F. Holby and D. Morgan, *Top. Catal.*, 2007, **46**, 285–305.

12 H. R. Colón-Mercado and B. N. Popov, *J. Power Sources*, 2006, **155**, 253–263.

13 S. Cherevko, G. P. Keeley, S. Geiger, A. R. Zeradjanin, N. Hodnik, N. Kulyk and K. J. J. Mayrhofer, *ChemElectroChem*, 2015, **2**, 1471–1478.

14 K. J. J. Mayrhofer, J. C. Meier, S. J. Ashton, G. K. H. Wiberg, F. Kraus, M. Hanzlik and M. Arenz, *Electrochem. commun.*, 2008, **10**, 1144–1147.

15 V. A. T. Dam, K. Jayasayee and F. A. de Bruijn, *Fuel Cells*, 2009, **9**, 453–462.

16 H. Schulenburg, B. Schwanitz, N. Linse, G. Scherer, A. Wokaun and F. Polytechnique, *J. Phys. Chem. C*, 2011, **115**, 14236–14243.

17 C. Galeano, J. C. Meier, V. Peinecke, H. Bongard, I. Katsounaros, A. a. Topalov, A. Lu, K. J. J. Mayrhofer and F. Schüth, *J. Am. Chem. Soc.*, 2012, **134**, 20457–20465.

18 R. M. Arán-Ais, Y. Yu, R. Hovden, J. Solla-Gullón, E. Herrero, J. M. Feliu and H. D. Abruña, *J. Am. Chem. Soc.*, 2015, **137**, 14992–14998.

19 S. Chen, H. A. Gasteiger, K. Hayakawa, T. Tada and Y. Shao-Horn, *J. Electrochem. Soc.*, 2010, **157**, A82.

20 K. Sasaki, N. Marinkovic, H. S. Isaacs and R. R. Adzic, *ACS Catal.*, 2016, **6**, 69–76.

21 A. A. Topalov, I. Katsounaros, M. Auinger, S. Cherevko, J. C. Meier, S. O. Klemm and K. J. J. Mayrhofer, *Angew. Chem. Int. Ed. Engl.*, 2012, **51**, 12613–5.

22 M. C. Smith, J. A. Gilbert, J. R. Mawdsley, S. Seifert and D. J. Myers, *J. Am. Chem. Soc.*, 2008, **130**, 8112–8113.

23 J. A. Gilbert, N. N. Kariuki, R. Subbaraman, A. J. Kropf, M. C. Smith, E. F. Holby, D. Morgan and D. J. Myers, *J. Am. Chem. Soc.*, 2012, **134**, 14823–14833.

24 J. L. R. Yates, G. H. Spikes and G. Jones, *Phys. Chem. Chem. Phys.*, 2015, **17**, 4250–4258.

25 M. K. Debe, *Nature*, 2012, **486**, 43–51.

26 L. Gancs, T. Kobayashi, M. K. Debe, R. Atanasoski and A. Wieckowski, *Chem.*

Mater., 2008, **20**, 2444–2454.

27 W. Liu, P. Rodriguez, L. Borchardt, A. Foelske, J. Yuan, A. K. Herrmann, D. Geiger, Z. Zheng, S. Kaskel, N. Gaponik, R. Kötz, T. J. Schmidt and A. Eychmüller, *Angew. Chemie - Int. Ed.*, 2013, **52**, 9849–9852.

28 A. I. Yanson, P. V. Antonov, Y. I. Yanson and M. T. M. Koper, *Electrochim. Acta*, 2013, **110**, 796–800.

29 A. I. Yanson, P. V. Antonov, P. Rodriguez and M. T. M. Koper, *Electrochim. Acta*, 2013, **112**, 913–918.

30 F. J. Vidal-Iglesias, J. Solla-Gullón, E. Herrero, V. Montiel, A. Aldaz and J. M. Feliu, *Electrochem. commun.*, 2011, **13**, 502–505.

31 J. Solla-Gullón, V. Montiel, A. Aldaz and J. Clavilier, *J. Electrochem. Soc.*, 2003, **150**, E104–E109.

32 J. Monzó, M. T. M. Koper and P. Rodriguez, *ChemPhysChem*, 2012, **13**, 709–715.

33 J. C. Meier, C. Galeano, I. Katsounaros, J. Witte, H. J. Bongard, A. A. Topalov, C. Baldizzone, S. Mezzavilla, F. Schüth and K. J. J. Mayrhofer, *Beilstein J. Nanotechnol.*, 2014, **5**, 44–67.

34 K. J. J. Mayrhofer, B. B. Blizanac, M. Arenz, V. R. Stamenkovic, P. N. Ross and N. M. Markovic, *J. Phys. Chem. B*, 2005, **109**, 14433–14440.

35 K. J. J. Mayrhofer, D. Strmcnik, B. B. Blizanac, V. Stamenkovic, M. Arenz and N. M. Markovic, *Electrochim. Acta*, 2008, **53**, 3181–3188.

36 Y. Garsany, I. L. Singer and K. E. Swider-Lyons, *J. Electroanal. Chem.*, 2011, **662**, 396–406.

37 S. Kocha, *DOE Annu. Prog. Rep.*, 2014, 215–218.

38 A. Ohma, K. Fushinobu and K. Okazaki, *Electrochim. Acta*, 2010, **55**, 8829–8838.

39 F. Hasché, M. Oezaslan and P. Strasser, *J. Electrochem. Soc.*, 2012, **159**, B24–B33.

40 K. Kinoshita and J. Bett, *Carbon N. Y.*, 1975, **11**, 403–411.

41 V. T. T. Ho, C. Pan, J. Rick, W. Su and B. Hwang, *J. Am. Chem. Soc.*, 2011, **133**, 11716–11724.

42 D. van der Vliet, D. S. Strmcnik, C. Wang, V. R. Stamenkovic, N. M. Markovic and M. T. M. Koper, *J. Electroanal. Chem.*, 2010, **647**, 29–34.

43 K. Ke, K. Hiroshima, Y. Kamitaka, T. Hatanaka and Y. Morimoto, *Electrochim. Acta*, 2012, **72**, 120–128.

44 M. Nesselberger, S. Ashton, J. C. Meier, I. Katsounaros, K. J. J. Mayrhofer and M. Arenz, *J. Am. Chem. Soc.*, 2011, **133**, 17428–17433.

45 Y. Liu, T. G. Kelly, J. G. Chen and W. E. Mustain, *ACS Catal.*, 2013, **3**, 1184–1194.

46 H. L. Xin, J. a Mundy, Z. Liu, R. Cabezas, R. Hovden, L. F. Kourkoutis, J.

Zhang, N. P. Subramanian, R. Makharia, F. T. Wagner and D. a Muller, *Nano Lett.*, 2012, **12**, 490–7.

47 S. C. S. Lai, R. A. Lazenby, P. M. Kirkman and P. R. Unwin, *Chem. Sci.*, 2014, **6**, 1126–1138.

48 A. Anastasopoulos, J. C. Davies, L. Hannah, B. E. Hayden, C. E. Lee, C. Milhano, C. Mormiche and L. Offin, *ChemSusChem*, 2013, **6**, 1973–1982.

Figure caption

Figure 1. (A, C) TEM image and XRD pattern of Pt-Nps. (B, D) TEM image and XRD pattern of Pt/TaC.

Figure 2. (A) Cyclic voltammograms in an Ar-saturated solution and (B) ORR polarization curves in O_2 satured solution of Pt-Nps (black), Pt/TaC (blue) and Pt/Vulcan (red) in 0.1 M $HClO_4$ at 20 mVs^{-1}. Rotation rate: ω = 1600 rpm.

Figure 3. Theoretical model of ECSA and Pt content evolution in a Pt degradation process. (Left panel) ECSA and Pt content evolution described for both (A) dissociative mechanism and (B) associative mechanism. (Right panel) Simplified representation of degradation mechanisms of platinum based catalyst.

Figure 4. Voltammetric profiles in 0.1 M $HClO_4$ of Pt-Nps (A), Pt/Vulcan (B) and Pt/TaC (C) at BOL (solid line) and EOL (dotted line). Scan rate υ = 50 mV s^{-1}. (D) ECSA (m^2 g^{-1}) as a function of cycle number.

Figure 5. Normalized ECSA, (solid symbols) and normalized Pt content, (open symbols) as a function of cycle number during the load cycle protocol. (A) Pt-Nps, (B) Pt/Vulcan and (C) Pt/TaC.

Figure 6. Positive-going ORR scan of (A) Pt-Nps, (B) Pt/Vulcan and (C) Pt/TaC at 0, 4000 and 10000 cycles. All the measurements were carried out in 0.1 M $HClO_4$ at 20 mVs^{-1}. Rotation rate: ω = 1600 rpm. (D) Normalized kinetic current density (*jk*, A mg^{-1}) at 0.9 V *vs.* RHE as a function of cycle number.

Figure 7. Voltammetric profiles of (A) Pt-Nps, (B) Pt/Vulcan and (C) Pt/TaC at BOL (solid line) and EOL (dotted line) in 0.1 M $HClO_4$ at 50 mV s^{-1}. (D) ECSA (m^2 g^{-1}) as a function of cycle number.

Figure 8. Normalized ECSA (solid symbols) and normalized Pt content (open symbols) as a function of cycle number during the start-up/shut-down protocol. (A) Pt-Nps, (B) Pt/Vulcan and (C) Pt/TaC.

Figure 9. Positive-going ORR scan of (A) Pt-Nps, (B) Pt/Vulcan and (C) Pt/TaC during the start-up/shut-down protocol. All the measurements were carried out in 0.1 M $HClO_4$ at 20 mVs^{-1}. Rotation rate: ω = 1600 rpm. (D) Normalized kinetic current density (*jk,* A mg^{-1}) at 0.9 V *vs.* RHE, as a function of cycle number.

Tables

Table 1. Summary of the initial conditions of the tree catalysts under study.

Catalyst	Pt	Pt/Vulcan	Pt/TaC
Particle size (nm)	5.2 ± 0.7	4.8 ± 0.1	5.2 ± 0.7
$Pt_{content}$ (wt. %)	100 ± 1.8	20.6 ± 1.1	19.6 ± 0.8
ECSA (m^2g^{-1})	53 ± 1	57 ± 1	54 ± 1
Specific activity (mA cm^{-2}) @0.9 V vs. RHE	0.482 ± 0.003	0.457 ± 0.002	0.65 ± 0.02
Mass activity (A mg^{-1}_{Pt}) @0.9 V vs. RHE	0.256 ± 0.002	0.256 ± 0.002	0.355 ± 0.001

Figures

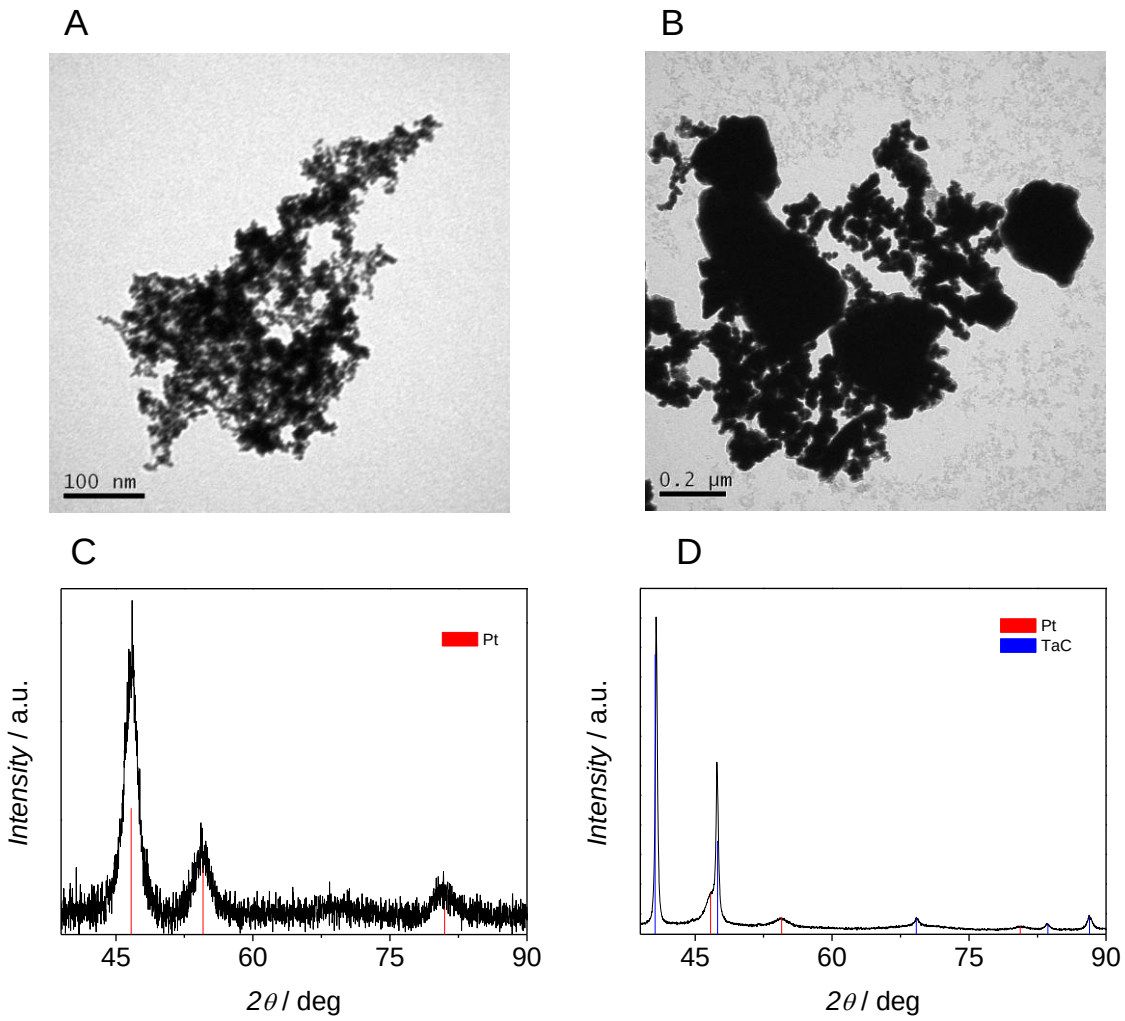

Figure 1

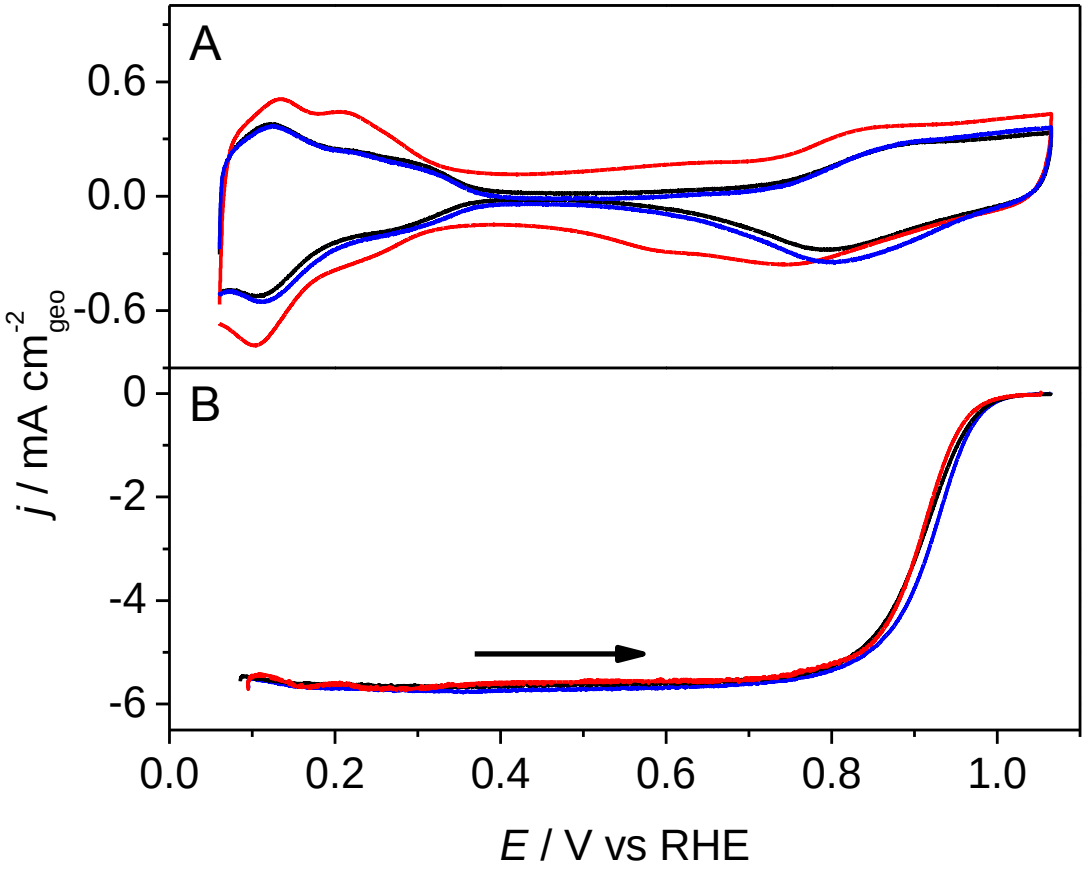

Figure 2

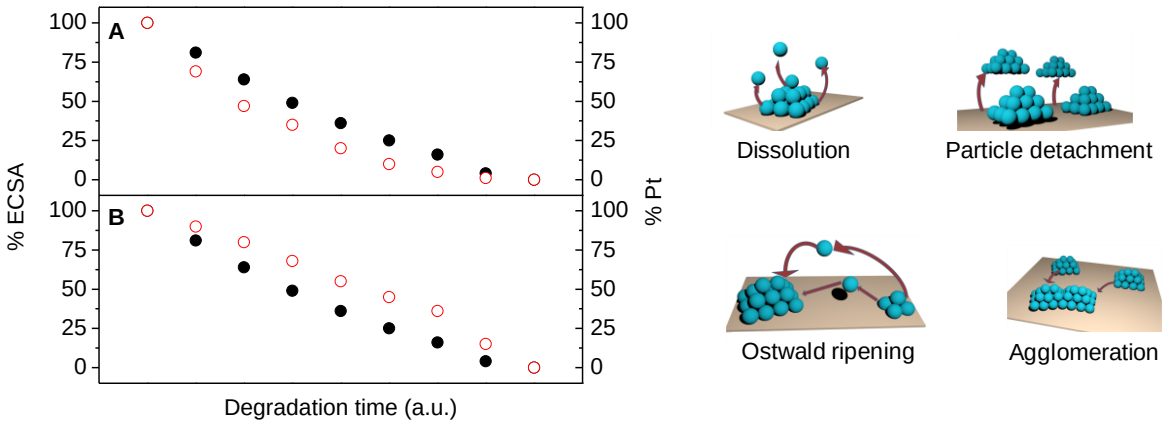
A
B
100
75
50
25
0
% ECSA
% Pt
Degradation time (a.u.)
Dissolution
Particle detachment
Ostwald ripening
Agglomeration

Figure 3

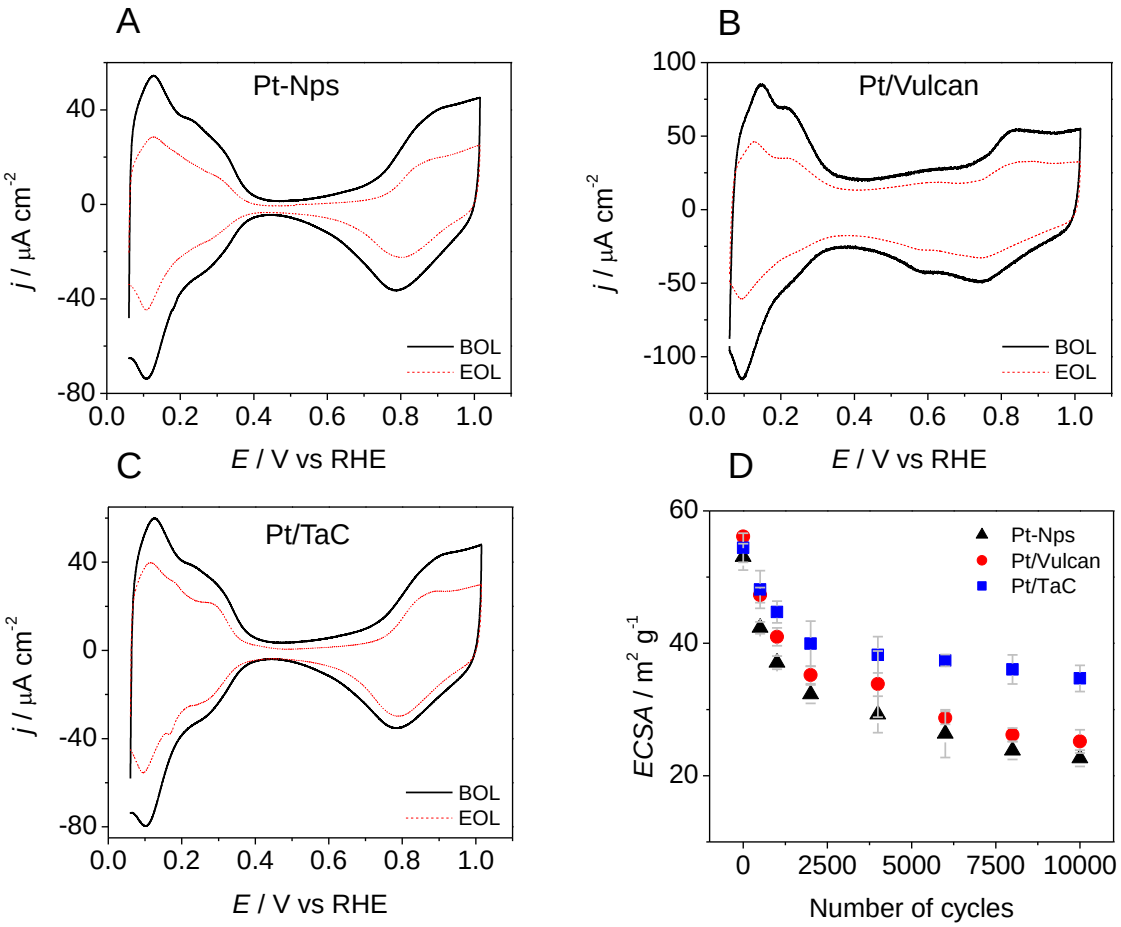
A
Pt-Nps
j / µA cm-2
E / V vs RHE
BOL
EOL
B
Pt/Vulcan
C
Pt/TaC
D
ECSA / m2 g-1
Number of cycles
Pt-Nps
Pt/Vulcan
Pt/TaC

Figure 4

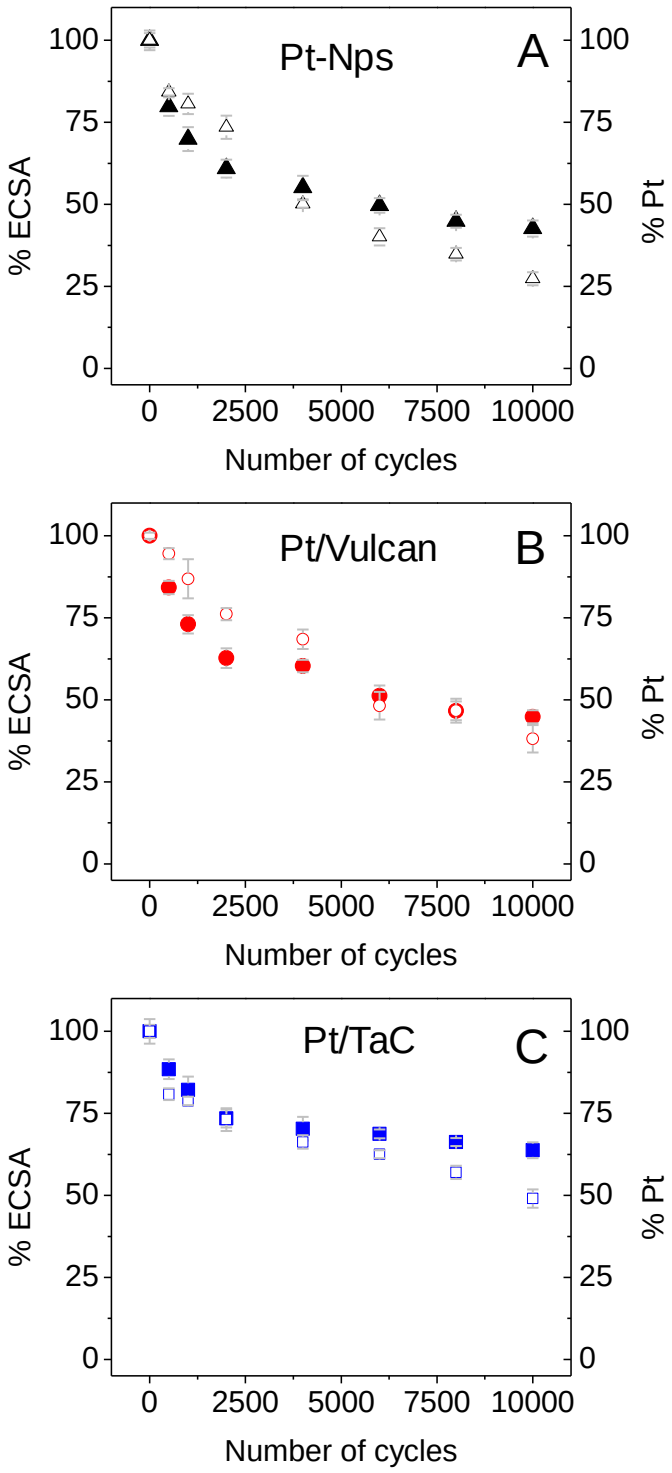
Pt-Nps
A
% ECSA
% Pt
Number of cycles
Pt/Vulcan
B
% ECSA
% Pt
Number of cycles
Pt/TaC
C
% ECSA
% Pt
Number of cycles
0
25
50
75
100
0
2500
5000
7500
10000

Figure 5

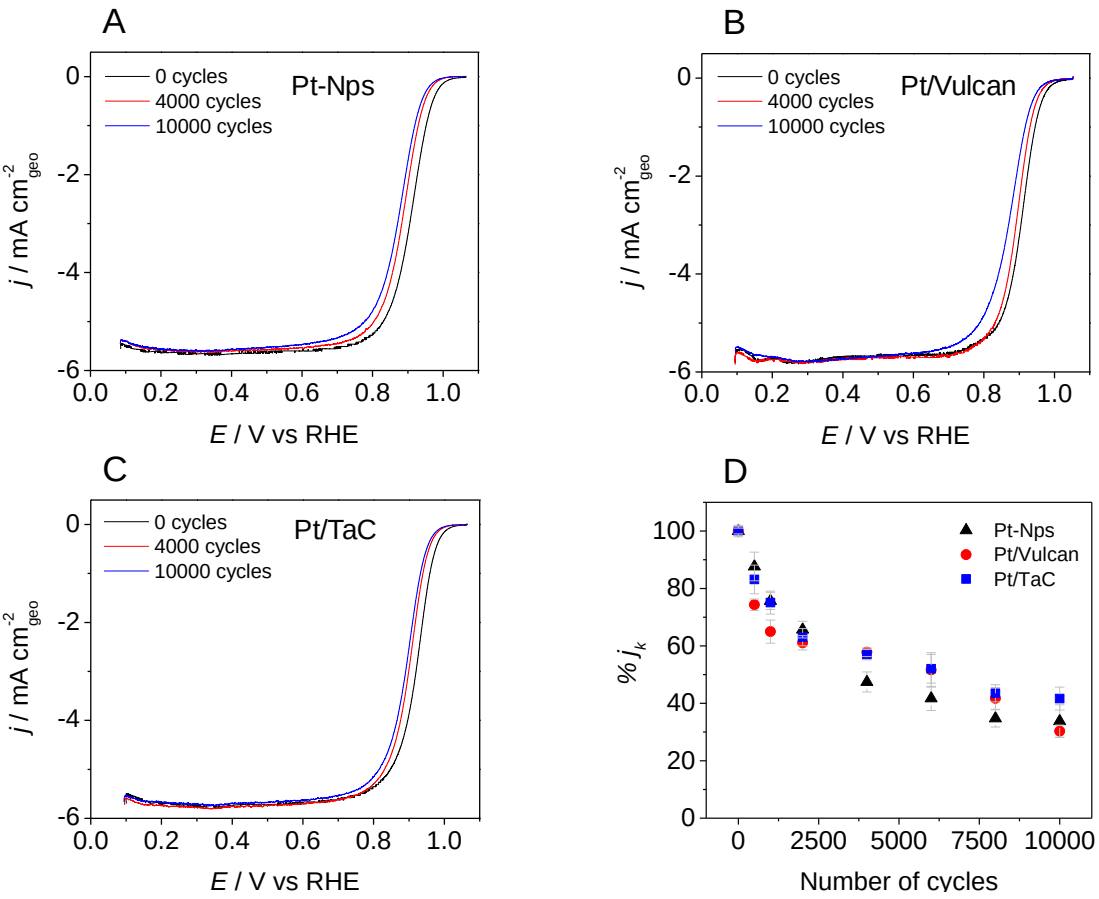
A
0 cycles
4000 cycles
10000 cycles
Pt-Nps
j / mA cm-2geo
E / V vs RHE
B
Pt/Vulcan
C
Pt/TaC
D
Pt-Nps
Pt/Vulcan
Pt/TaC
% jk
Number of cycles

Figure 6

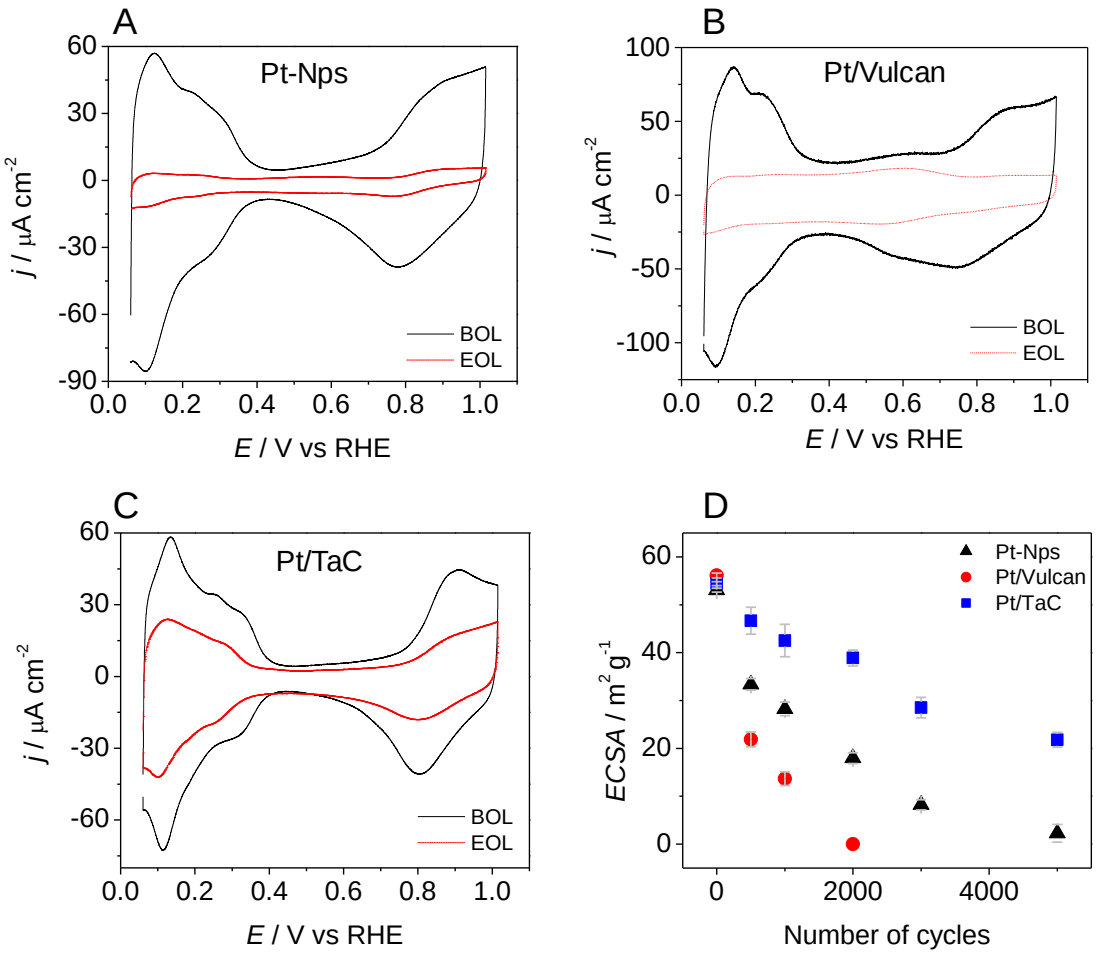
A
Pt-Nps
BOL
EOL
j / µA cm-2
E / V vs RHE
B
Pt/Vulcan
BOL
EOL
j / µA cm-2
E / V vs RHE
C
Pt/TaC
BOL
EOL
j / µA cm-2
E / V vs RHE
D
Pt-Nps
Pt/Vulcan
Pt/TaC
ECSA / m2 g-1
Number of cycles

Figure 7

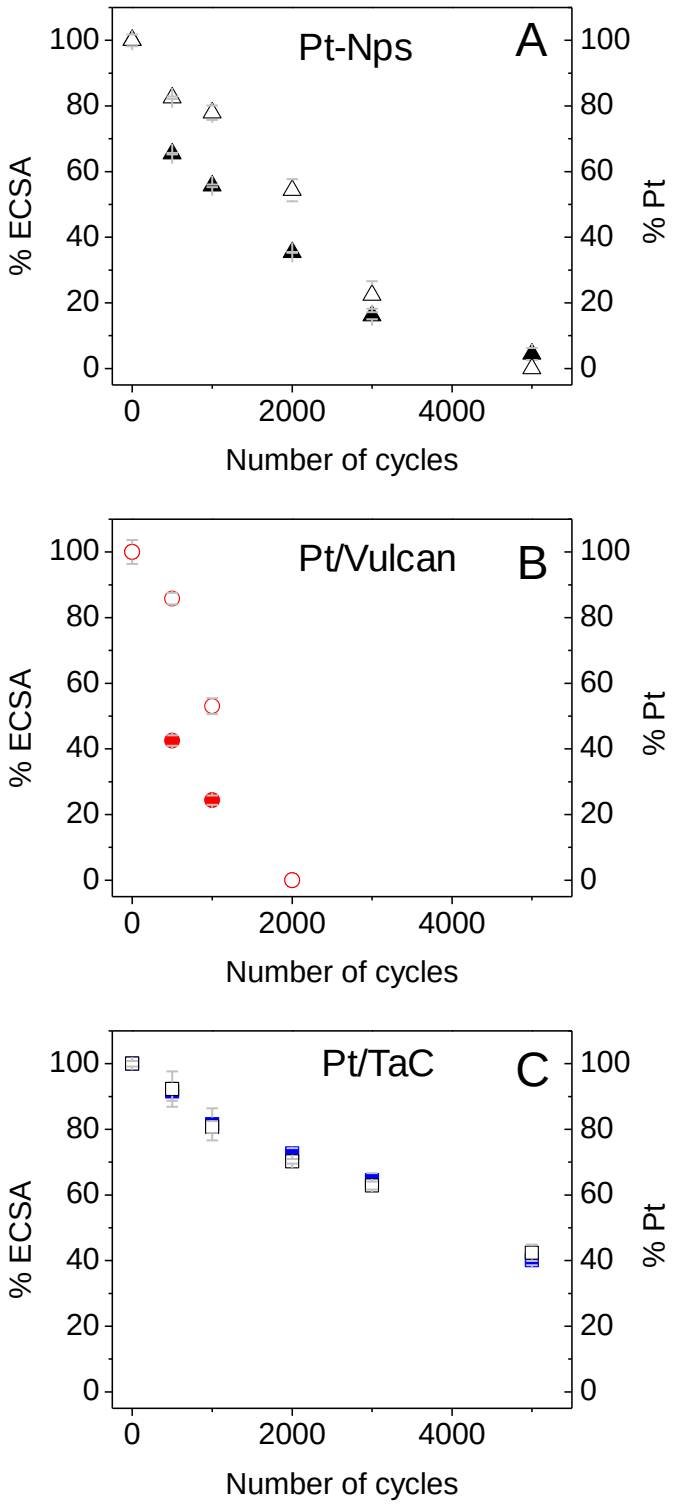
Pt-Nps
A
Pt/Vulcan
B
Pt/TaC
C
% ECSA
% Pt
Number of cycles
0
20
40
60
80
100
0
2000
4000

Figure 8

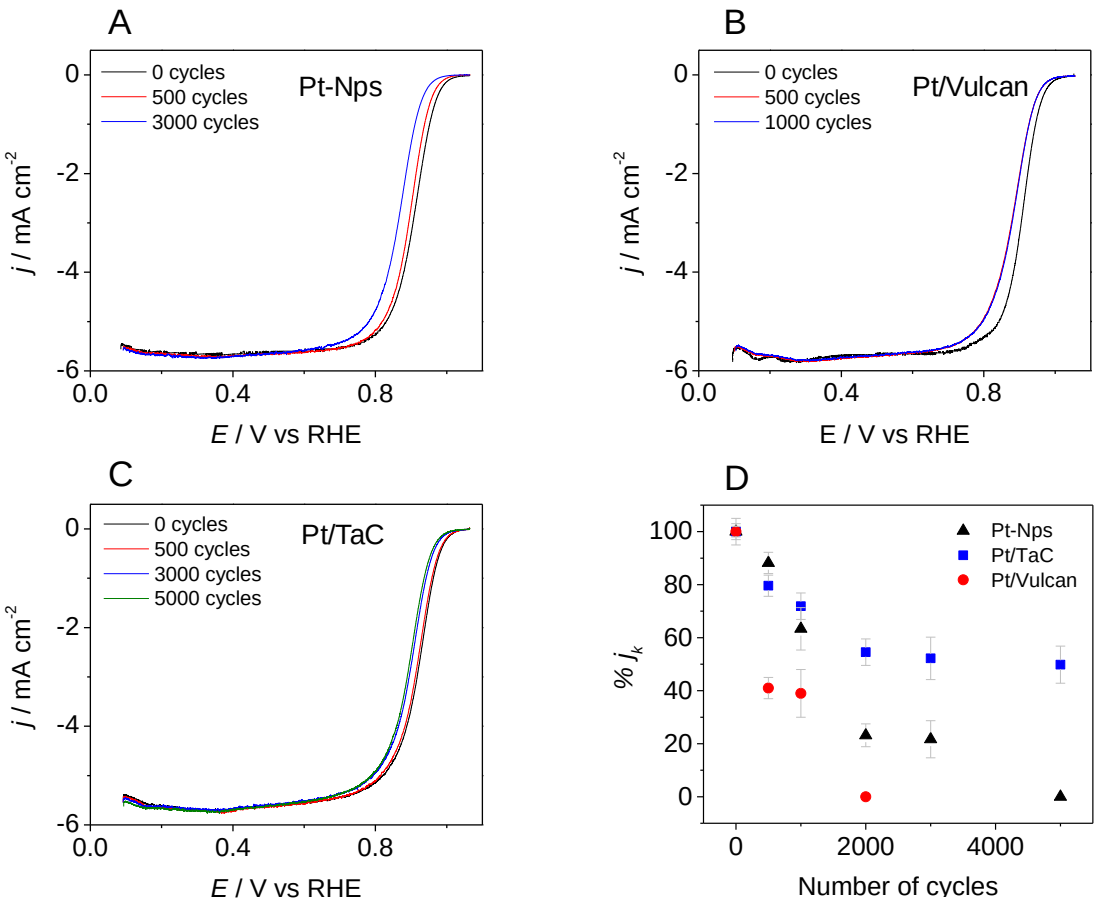
A
0 cycles
500 cycles
3000 cycles
Pt-Nps
j / mA cm-2
E / V vs RHE
B
0 cycles
500 cycles
1000 cycles
Pt/Vulcan
j / mA cm-2
E / V vs RHE
C
0 cycles
500 cycles
3000 cycles
5000 cycles
Pt/TaC
j / mA cm-2
E / V vs RHE
D
Pt-Nps
Pt/TaC
Pt/Vulcan
% jk
Number of cycles

Figure 9